Modulation of amyloidogenic protein self-assembly using tethered small molecules

Emma E. Cawood[a,b,c], Nicolas Guthertz[a,c], Jessica S. Ebo[a,c], Theodoros K. Karamanos[a,c,d], Sheena E. Radford[a,c]*, Andrew J. Wilson[a,b]*

[a]Astbury Centre for Structural Molecular Biology, University of Leeds, Leeds LS2 9JT, United Kingdom

[b]School of Chemistry, University of Leeds, Leeds LS2 9JT, United Kingdom

[c]School of Molecular and Cellular Biology, University of Leeds, Leeds LS2 9JT, United Kingdom

[d]Laboratory of Chemical Physics, National Institute of Diabetes and Digestive and Kidney Diseases, National Institutes of Health, Bethesda, Maryland, United States

ABSTRACT

Protein-protein interactions (PPIs) are involved in many of life's essential biological functions yet are also an underlying cause of several human diseases, including amyloidosis. The modulation of PPIs presents opportunities to gain mechanistic insights into amyloid assembly, particularly through the use of methods which can trap specific intermediates for detailed study. Such information can also provide a starting point for drug discovery. Here, we demonstrate that covalently tethered small molecule fragments can be used to stabilize specific oligomers during amyloid fibril formation, facilitating the structural characterization of these assembly intermediates. We exemplify the power of covalent tethering using the naturally occurring truncated variant (ΔN6) of the human protein β2-microglobulin (β2m), which assembles into amyloid fibrils associated with dialysis-related amyloidosis. Using this approach, we have trapped tetramers formed by ΔN6 under conditions which would normally lead to fibril formation and found that the degree of tetramer stabilization depends on the site of the covalent tether and the nature of the protein-fragment interaction. The covalent protein-ligand linkage enabled structural characterization of these trapped oligomeric species using X-ray crystallography and NMR, providing insight into why tetramer stabilization inhibits amyloid assembly. Our findings highlight the power of "post-translational chemical modification" as a tool to study biological molecular mechanisms.

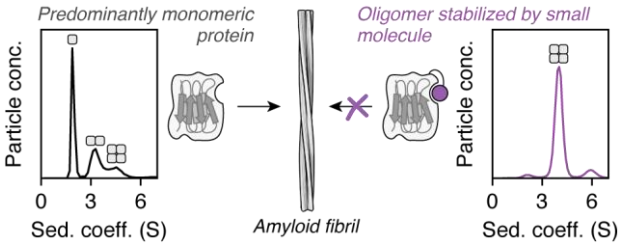

INTRODUCTION

The regulated self-assembly of proteins into ordered complexes drives many biological processes, ranging from viral capsid formation and actin polymerization, to DNA maintenance and repair[1,2]. However, self-assembly can also occur aberrantly as a result of changes in the concentration[3], environment[4–6], primary sequence[7,8], or post-translational processing[9–11] of a protein. Aberrant assembly events are associated with a range of disorders, and can involve polymerization of natively folded protein molecules[2], as in sickle cell anemia[12], or aggregation which is accompanied by significant conformational changes, as exemplified by amyloid diseases[13,14]. Understanding the molecular basis and consequences of such protein-protein interaction (PPI) pathways and identifying methods for their modulation[15–20] therefore has implications for the treatment of disease[21], as well as in the development of new biomaterials, where protein self-assembly can be exploited to yield structures with defined architectures or novel biomechanical properties[22,23]. However, manipulating and defining the mechanisms of self-assembly is challenging, due to the transient nature and heterogeneity (in mass and structure) of oligomeric intermediates[24,25]. The use of methods to trap specific oligomeric complexes can help overcome these challenges and offers the opportunity to structurally characterize otherwise transient intermediates, identify targets for drug discovery, and develop new scaffolds for protein-based nanostructures.

Here, we describe the use of disulfide tethering[26] to rapidly explore chemical space and identify "post-translational chemical modifications"[27,28] that stabilize specific PPIs associated with amyloid assembly. These site-specific, covalent modifications may act in one of two ways: altering the surface properties of the protein and/or covalently reinforcing a non-covalent protein-ligand interaction. Using a naturally occurring, amyloidogenic variant of β_2-microglobulin (β_2m) – the ΔN6 variant – as a model system, we show that covalently tethered fragments represent highly effective tools for tuning oligomer populations and stabilizing particular species in self-assembly pathways. The covalent modifications identified here have led to structural and functional insights into the role of tetramers in ΔN6 amyloid formation, notably from analysis of a crystal structure of this small molecule-stabilized oligomer.

Native monomeric β_2m has a seven-stranded immunoglobulin fold and forms the non-covalently bound light chain of the major histocompatibility class I complex[29]. Aberrant self-assembly of β_2m molecules into amyloid fibrils[30] is a hallmark of dialysis-related amyloidosis (DRA)[31–33]. The amyloidogenic variant of β_2m which is the focus of this paper – ΔN6 – is formed from the wild-type protein by proteolysis of its N-terminal six amino acids and makes up ~20-30% of β_2m molecules found in fibrils extracted from DRA patients[34,35]. ΔN6 is capable of rapid assembly into amyloid fibrils *in vitro* at near-neutral pH, through the association of the dynamically-structured monomers[36] into dimers and hexamers that retain a native-like fold[37] (Figure 1A). Subsequent conformational rearrangement of these oligomers into cross-β structures leads to amyloid fibril formation and elongation[38].

Recent structural models of ΔN6 dimers and hexamers have shown that the DE and BC loops of the protein are involved in both oligomerization interfaces (Figure 1A)[37]. The same regions have also been identified at the interface of amyloid-competent ΔN6-β_2m heterodimers[39], β_2m-β_2m homodimers[40], and inhibitory heterodimers formed between ΔN6 and a non-amyloidogenic β_2m ortholog (murine β_2m)[39]. These examples implicate the DE and BC loops, and thereby also the associated β strands, as mediators of oligomerization, and thus targeting these regions (e.g. by small molecules) was anticipated to yield tools for controlling and studying ΔN6 self-assembly. The dynamic nature of ΔN6 monomers[36] and oligomers[37] has, thus far, hindered the development of small molecule modulators of amyloid formation (although protein-based modulators have been identified[41]). In light of this challenge, we focused our efforts on the development of covalent ligands to manipulate ΔN6 self-assembly, based on the success of such compounds in targeting other challenging PPIs[42–44].

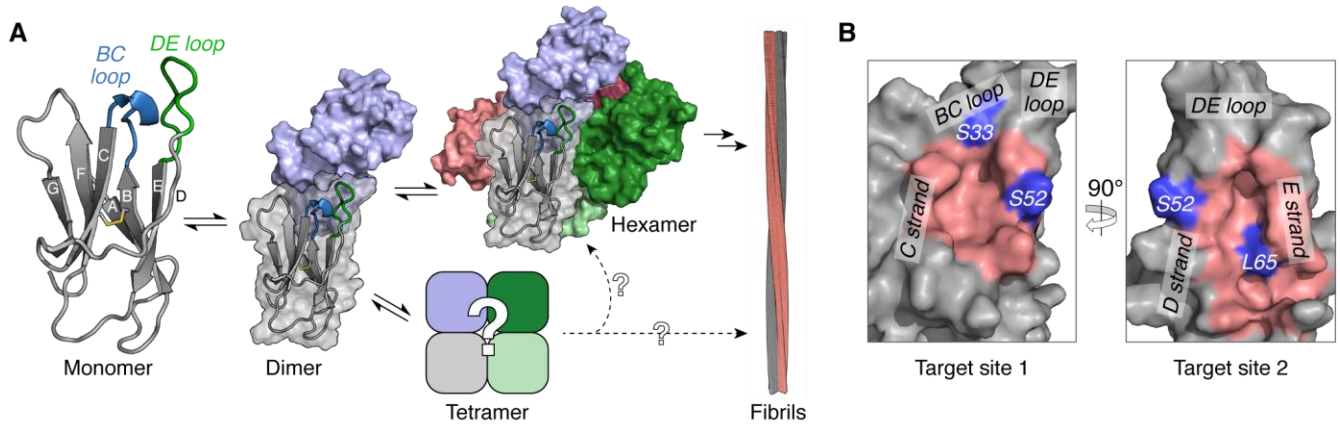

Figure 1. **A**: Native monomeric ΔN6 (PDB 2XKU[36]) contains seven antiparallel β-strands (labelled A-G), with a solvent-excluded disulfide bond between strands B and F (yellow). The monomeric protein is capable of associating into transient, native-like dimers and hexamers *en route* to amyloid fibrils (structures not drawn to scale)[37]. The conversion of these native-like oligomers into fibrils requires structural rearrangement of the existing β-strands[38] and further self-assembly. ΔN6 tetramers have been observed but their structure and role in fibril formation appear to depend on solution conditions[37,45]. **B**: The two most ligandable sites (pink) of ΔN6 identified by computational solvent mapping were found to be located adjacent to the BC (target site 1) and DE (target site 2) loops. Three residues (S33, S52 and L65; purple) at these two sites were substituted with cysteine in order to target each pocket using the disulfide tethering strategy (see Figure 2A). The orientation of ΔN6 in the 'Target site 1' panel is the same as for the monomer shown in Figure 1A.

RESULTS AND DISCUSSION

Identifying covalent ligands for ΔN6 by disulfide tethering. Computational solvent mapping (using the FTMap server[46]) was performed against an NMR-derived conformational ensemble of ΔN6[36] in order to predict which regions of the protein are likely to be hot spots for small molecule binding. The resulting data (Figure S1) highlighted two pockets adjacent to the DE and BC loops as promising targets for ligand development (site 1 and site 2, Figure 1B). To identify possible covalent ligands for these sites, a library of small molecules was screened using the 'disulfide tethering' method[26] (Figure 2A). First developed by Erlanson and co-workers as a site-directed screening strategy[47], this approach uses disulfide bonds to covalently trap and assess the interaction affinity of small molecules (typically fragments) which have bound non-covalently to the protein of interest. Libraries of disulfide-functionalized molecules are screened for their ability to form disulfide bonds with cysteine variants of the target protein, as small molecules which exhibit favorable non-covalent interactions near the free, solvent-exposed cysteine residue will undergo thiol-disulfide exchange more effectively due to their increased local concentration. The relative population of different covalent complexes at equilibrium can therefore be used as a proxy for the non-covalent affinity of a given fragment for a particular region of the target protein.

Three single cysteine variants of ΔN6 (S33C, S52C, and L65C; Figure 1B) were expressed and purified (Figure S2) in order to monitor small molecule binding at sites 1 and 2 using the disulfide tethering approach. A library of 76 symmetrical disulfides (designed with the aid of molecular docking, as described in the Supporting Information) was prepared using solid-phase synthesis (Figure S3) and screened against each ΔN6 cysteine variant in cocktails of five, in the presence of excess reducing agent (β-mercaptoethanol; βME). The relative populations of the different protein-fragment adducts were assessed at 24 h by electrospray ionization mass spectrometry and normalized as robust Z (RZ) scores[48] (Figure 2B; Figures S4-S7), where higher RZ scores were anticipated to reflect more favorable protein-fragment interactions (Figure 2A). Comparison of the distribution

of protein-fragment adducts observed for the three ΔN6 cysteine variants to that of an unrelated, largely helical control protein, MCL-1, showed that there was poor correlation between most data sets (median r = 0.38; Figure S6) and therefore that the identity of the protein affects which protein-fragment adducts dominate at equilibrium. This observation suggests that the preference of ΔN6 for particular fragments (as shown in Figure 2B) was a result of specific non-covalent interactions. RZ scores were therefore used to report on the relative non-covalent affinities of tethered fragments for a particular region on the surface of ΔN6.

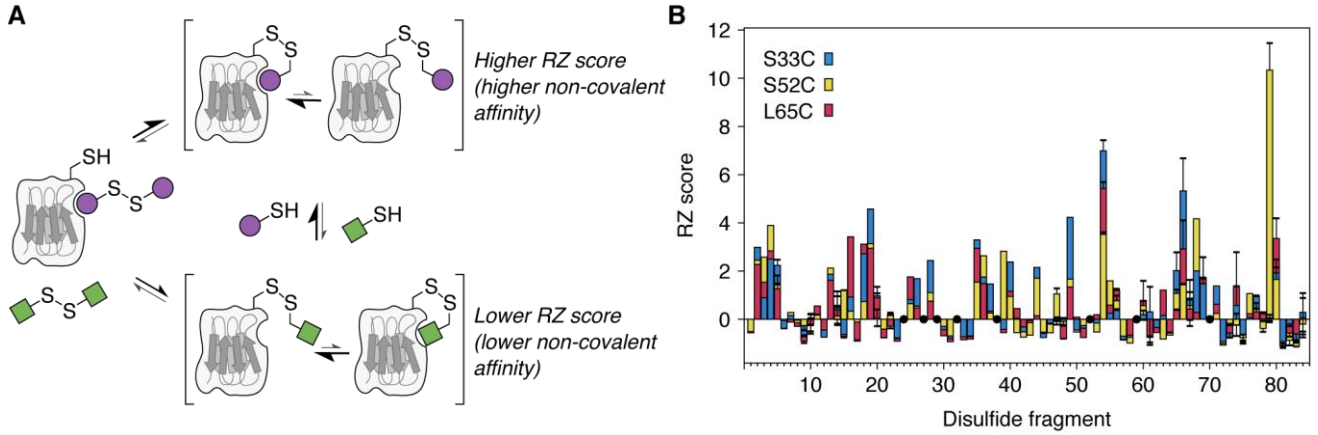

Figure 2. A: A schematic representation of the disulfide tethering method used to compare non-covalent affinities of different fragments for specific target sites on ΔN6. When using cocktails of fragments, the compound which forms the most favorable non-covalent interactions with the target protein while tethered by a disulfide bond will produce the most stable (i.e. highest populated) covalent protein-fragment adduct at equilibrium – this is reflected by a higher RZ score. **B:** Data from a disulfide tethering screen against three ΔN6 cysteine variants (S33C, S52C, and L65C) normalized as RZ scores. For fragments which were present in more than one screening cocktail, data are shown as the mean ± one standard deviation. Each cysteine variant was present at 5 μM and was incubated for 24 h with 25 μM of each disulfide-linked fragment (in cocktails of 5 fragments) and 500 μM βME, in 25 mM sodium phosphate pH 6.2, 2% v/v DMSO. Black circles are shown for fragments which were synthesized but not included in the screening library due to poor purity.

Covalent functionalization and ligand binding around the DE/BC loops drive ΔN6 tetramerization. To interrogate how covalent modification of different regions of ΔN6 affects aggregation, sedimentation velocity analytical ultracentrifugation (SV-AUC) was used to assess the oligomeric state of a series of individual protein-fragment adducts (Figure 3A; Figures S8-S10). Fragments with a range of RZ scores were selected for testing with each cysteine variant, so as to distinguish between changes in oligomeric state which were due to covalent modification of the protein (i.e. changes observed for all samples of a given cysteine variant) versus changes which arose from specific non-covalent protein-ligand interactions (i.e. those observed only for covalently tethered fragments with high RZ scores).

In the absence of covalent modification, ΔN6 is approximately 50% monomeric under the conditions employed (150 μM protein, pH 6.2, 25 °C), with dimers, tetramers, and hexamers representing the majority of faster sedimenting species (Figure S2), consistent with previous reports[37]. Tethering of high RZ score fragments to all three ΔN6 cysteine variants was found to increase the population of tetramers (representative data in Figure 3B, 3D; see also Figures S11-S13). Tethering with low RZ score fragments, however, produced a variety of results, which depended both on the cysteine variant and the ligand employed.

For L65C-fragment adducts, the area of the tetramer peak in the continuous sedimentation coefficient ($c(s)$) distributions showed a positive correlation with the RZ score of the tethered fragment (Figure 3C; Figures S13, S14): a covalently attached fragment with a low RZ score (βME) produced an oligomer distribution which was similar (albeit not identical) to that of ΔN6 alone (tetramer peak areas of 5% and 18%, respectively), while tethered fragments with high RZ scores produced significantly

larger tetramer peaks (e.g. a 45% tetramer peak area was observed for the adduct between L65C and disulfide **54** – named L65C-S**54**) (Figure 3B, 3C). The only predicted ligandable pocket that is near residue 65 of ΔN6 is target site 2 (Figure 1B), suggesting that the formation of tetramers by L65C-fragment adducts is driven by non-covalent binding to this pocket.

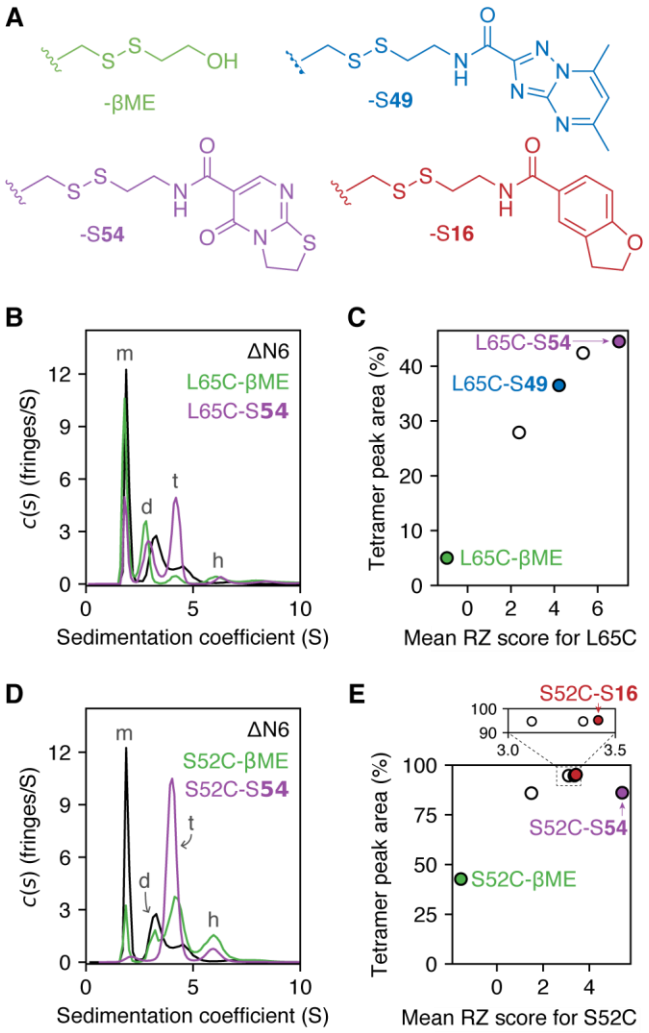

Figure 3. A: Examples of fragments used to form the S52C- and L65C-fragment adducts studied by SV-AUC. **B-E**: SV-AUC data collected for L65C-fragment adducts (**B**, **C**) or S52C-fragment adducts (**D**, **E**). Experiments were performed with 150 μM protein in 25 mM sodium phosphate at pH 6.2, 25 °C. Peaks in the *c*(*s*) distributions were assigned to monomer (m), dimer (d), tetramer (t), or hexamer (h), based on previous studies[37] and predicted sedimentation coefficients for these oligomers (calculated using the Svedberg equation[49]). Tetramer peak areas for a range of L65C-fragment adducts were found to correlate with the RZ score of the attached fragment (**C**). The relationship between fragment RZ score and tetramer peak area for S52C-fragment adducts was less clear, and other properties of the fragments may play a role in modulating tetramer populations (**E**) (see Figure S14).

The nature of the relationship between tetramer population and fragment RZ score for the S52C- and S33C-fragment adducts was less clear. All S52C-fragment adducts produced tetramer peak areas ≥ 43% (with most between 86-95%), regardless of RZ score (Figure 3D, 3E; Figures S12, S14), implying that a different property of the fragments was driving the changes in oligomeric state. Although a limited range of fragment sizes were used in screening, the observed tetramer populations for the different S52C-fragment adducts are consistent with fragment size (and thus the surface topography of protein-fragment adducts) being a contributing factor (Figure S14). The S33C-fragment adducts analyzed were generally polydisperse, with only two samples (of seven analyzed) producing *c*(*s*) distributions which were readily interpretable (Figure S11): S33C-βME and

S33C-S**79**, the latter of which showed an increased tetramer peak area (43%) over the former (16%). These data are insufficient to ascertain which characteristic(s) of the covalent fragments influence the tetramer population of S33C-fragment adducts, but further emphasize that, as for L65C and S52C, the addition of specific covalent fragments to S33C can be used to modulate oligomer distributions.

Tetramer stabilization inhibits amyloid assembly. The ability of covalently tethered fragments to generate defined oligomer populations offered the opportunity to explore the effect of tetramer stabilization on ΔN6 amyloid assembly. Protein-fragment adducts with a range of tetramer populations were added to pre-formed ΔN6 amyloid fibrils, and the ability of these samples to elongate the fibril seeds was analyzed using the fluorescent, fibril-binding dye, thioflavin T (ThT)[50,51]. By using this strategy, fibril elongation by each sample will be templated by seeding to a common fibril product, irrespective of the covalent ligand, enabling direct comparison of the initial rates of fibril growth for different protein-fragment adducts. It should be noted that under the conditions employed, spontaneous (i.e. unseeded) fibril formation does not occur on the timescale of the experiment.

For all three ΔN6 cysteine variants, the observed elongation rates were lower for samples with higher tetramer populations (Figure 4; Figure S15A-B). The most dramatic change in fibril elongation was seen for S52C-S**54** (86% tetramer peak area in the *c*(*s*) distribution), where the rate of elongation was reduced more than 30-fold relative to ΔN6 (Figure 4E). Global linear regression analysis across all samples showed that there is a negative correlation (r = -0.78) between fibril elongation rates and tetramer populations, and extrapolation of the linear regression line to 100% tetramer corresponds precisely to an elongation rate of zero (Figure S15B). Together, these observations indicate that the tetramers formed by the S33C-, S52C-, and L65C-fragment adducts lie off-pathway to amyloid fibril formation. Prediction of elongation rates using kinetic schemes in which tetramers lie on- or off-pathway to fibrils also supports this conclusion (Figure S16). The fibril elongation data thus highlight tetramer stabilization as a strategy to inhibit ΔN6 amyloid formation. In addition, they support a model in which covalent functionalization and covalent reinforcement of ligand binding around the DE and BC loops can be used to slow the progression of seeded amyloid formation by modulating the stability and population distribution of oligomers.

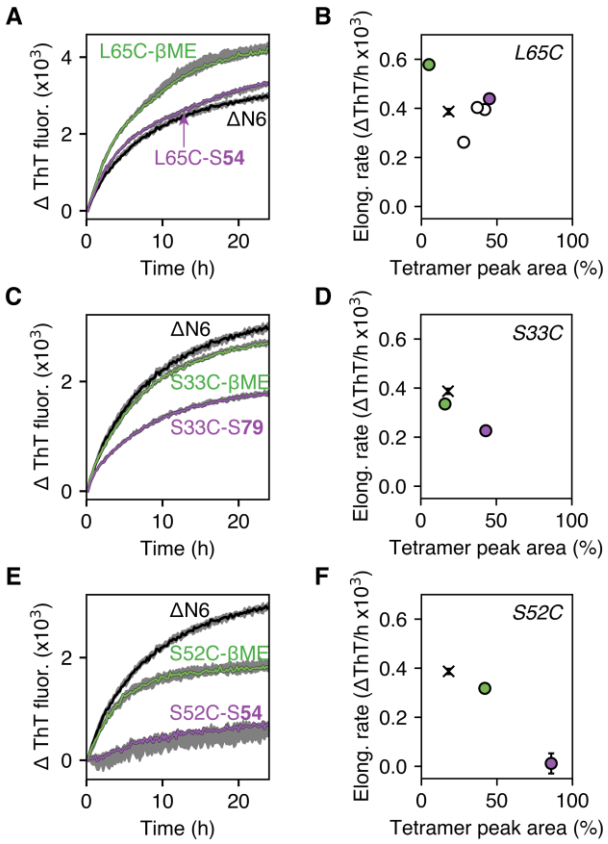

Figure 4. The change in ThT fluorescence over time for various protein-fragment adducts (150 μM) in the presence of ΔN6 fibril seeds (15 μM monomer equivalents) shows that the ability of samples to elongate fibrils (**A**, **C**, **E**) depends on the tetramer population (**B, D, F**). Data in **A**, **C**, and **E** are shown as the median curve, with the highest and lowest values shaded in grey (n = 3). Error bars (standard deviation) are shown for all data points (mean values) in **B**, **D**, and **F** – those error bars which are not visible are smaller than the displayed data point. Additional ThT fluorescence curves associated with **B** which were not shown in **A** (i.e. the white circles in **B**) are shown in Figure S15A. All experiments were performed under quiescent conditions in 25 mM sodium phosphate pH 6.2, 25 °C. Elongation rates for unliganded ΔN6 are shown by black crosses in **B**, **D**, and **F**.

Structural characterization of stabilized tetramers. To understand how the tetramers generated by the covalent modification of ΔN6 are structurally related to the previously characterized dimers and hexamers[37], and how and why covalent modification around the DE and BC loops leads to tetramerization, X-ray crystallography and solution-state structural studies were performed.

S52C-S**54** was found to crystallize as a ring-shaped tetramer with a solvent-accessible central cavity, formed from two asymmetric units each containing two ΔN6 molecules in an antiparallel orientation (Figure 5A-C; Table S1). As seen for the on-pathway ΔN6 dimer and hexamer[37], the protein subunits in the crystallized tetramer are highly native-like, but notably with perturbations to the DE and BC loops, and a shift of the D strand from a β-bulge to a straight β-strand (Figure 5D; Figure S17A). These structural changes appear to be linked to each other and to tetramerization: straightening of the D strand allows for protein-protein interactions to occur via β-sheet augmentation, forming one of the two interaction interfaces in the tetramer (Figure 5B), and additionally results in a rearrangement of phenylalanine residues at the top of the D, E, and B strands (Phe56, Phe62, and Phe30, respectively) which is accommodated by rearrangement of the BC loop (Figure S17B). The movement of residues around the BC and DE loops which accompanies D strand straightening allows several key protein-protein contacts

to be made within the second interaction interface, which occurs through a face-to-face, antiparallel interaction of the ABED β-sheets (Figure 5C; Figure S17C).

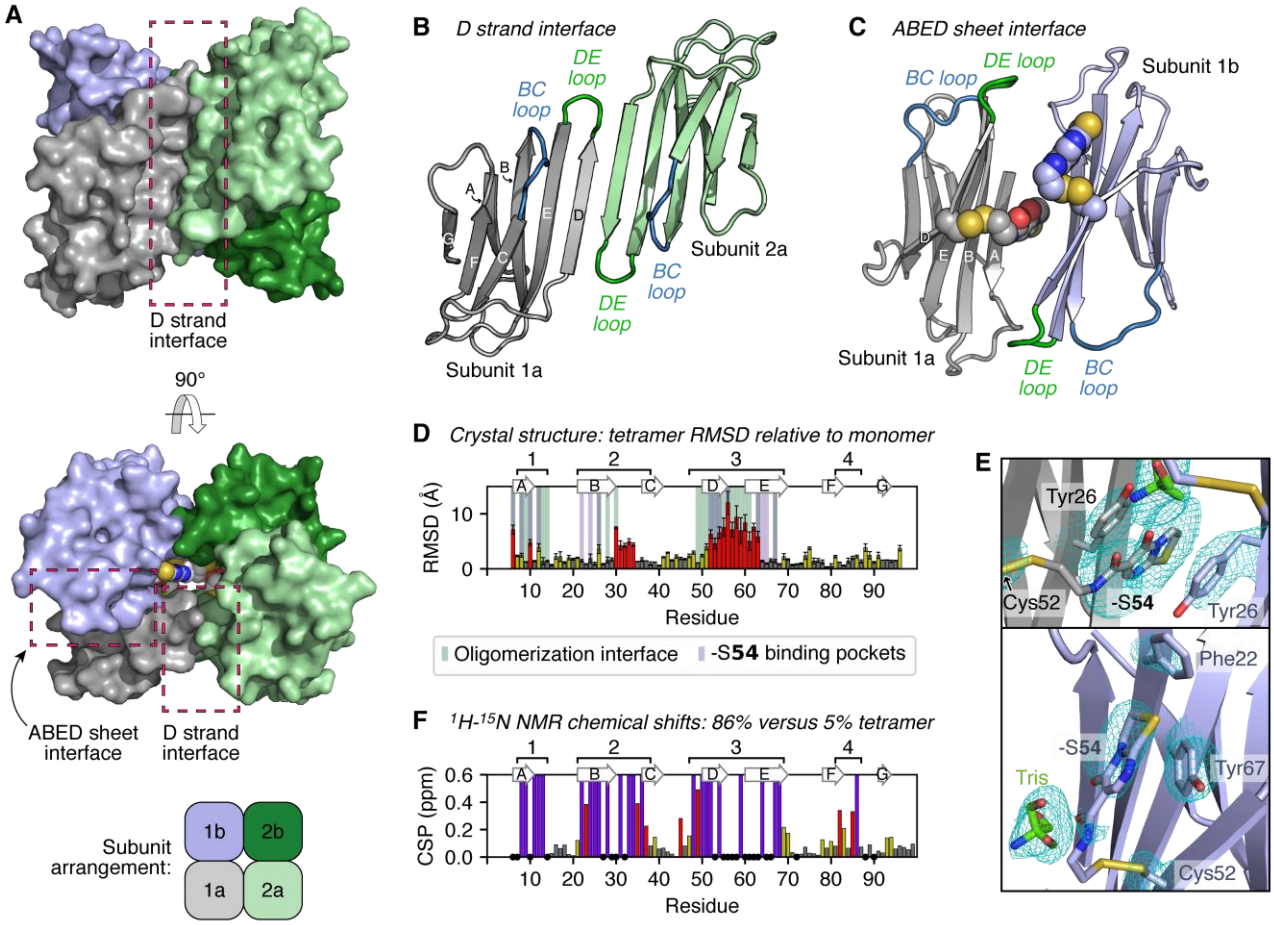

Figure 5. **A-C:** Crystal structure of the S52C-S**54** tetramer (diffracted to 2.4 Å; PDB 7AFV), formed from two asymmetric units (subunits 1a/1b and subunits 2a/2b). Protein subunits interact via two interfaces: the D strand interface (**B**) and the ABED sheet interface (**C**). Four copies of the covalent -S**54** fragment (shown as spheres in **A** and **C**) are present in this complex and lie within the ABED sheet interface, in a central solvent-accessible cavity (**C**). **D:** Per-residue RMSD values for the S52C-S**54** tetramer crystal structure (subunit 1a/2a) compared to the monomeric ΔN6 NMR ensemble (30 structures; PDB 2XKU[36]), reported for all non-hydrogen atoms. Values are shown as the mean RMSD (± standard deviation) across the monomeric NMR ensemble. Residues which are ≤ 6 Å from another protein subunit or a -S**54** fragment within the S52C-S**54** tetramer structure are additionally highlighted by green or purple bars, respectively. The locations of the β-strands in the S52C-S**54** tetramer crystal structure are shown above the plot. **E:** Each -S**54** fragment can bind in one of two binding sites around the site 2 pocket: by π-stacking between two Tyr26 residues within the ABED sheet interface or by π stacking against Tyr67. The 2Fo-Fc electron density map (contoured at 1.1σ) is shown in cyan for the displayed amino acid sidechains and organic molecules. **F:** Combined ^{1}H-^{15}N chemical shift differences between S52C-S**54** and L65C-βME HMQC NMR spectra – these samples had tetramer peak areas of 86% and 5%, respectively, in their *c*(*s*) distributions. Residues which were not visible (or could not be confidently assigned based on comparison to previous ΔN6 assignments[36]) for either sample are shown as black circles. Residues which were visible for L65C-βME but were broadened beyond detection for S52C-S**54** are shown by purple bars. Resonances which were visible in both spectra are colored according to the magnitude of the chemical shift perturbation (CSP) relative to the standard deviation of the data set (σ): CSP ≥ 2σ, red; σ ≤ CSP < 2σ, yellow; CSP < σ, grey. Four main regions (labelled 1-4) show either significant changes in the position of ^{1}H-^{15}N resonances or complete loss of these resonances in samples with higher tetramer populations (see Figure S21).

Clear electron density indicated the presence of four covalently bound -S**54** fragments within the central cavity of the tetramer (Figure 5A; bottom structure) which make intra- and/or inter-subunit contacts with the site 2 pocket of surrounding protein subunits (Figure 5E; Figure S17C). The protein-ligand interactions with the strongest electron density, and which are therefore the interaction which presumably contributes most to the stabilization of the tetramer, involve π stacking between two Tyr26 residues within the ABED sheet interface and the bicyclic ring system of a fragment **54** molecule (grey ligand in Figure 5E) – this arrangement is seen for two of the four fragments in a tetramer. These protein-ligand interactions may additionally stabilize the straight conformation of the D strand – residue 52 lies too far away from Tyr26 in the monomeric ΔN6 structure for this interaction to occur and thus this protein-ligand interaction can only form when the D strand is straight (Figure S17D). Therefore, while no direct protein-ligand contacts occur with either the DE or BC loops, contacts with the associated β-strands appear to have driven conformational changes in these regions, via changes in the associated β-strands, and together these structural changes have altered the ΔN6 self-assembly landscape. The electron density associated with the remaining two fragments in the tetramer is not as well defined as for those intercalated between Tyr26 residues but appear to reflect a binding mode whereby the fragments can form intra-subunit π-π interactions with Tyr67 residues (Figure 5E, pale blue ligand).

^{1}H-^{15}N HMQC NMR spectra and ^{15}N-relaxation measurements acquired for various S52C- and L65C-fragment adducts were consistent with the tetramer observed within the S52C-S**54** crystal lattice, implying that this crystal structure reflects the nature of these off-pathway ΔN6 tetramers in solution (Figures S18-S21). Comparison of the chemical shifts and intensities of ^{1}H-^{15}N backbone amide resonances between samples with higher tetramer populations (e.g. S52C-S**54** and L65C-S**54**) and those with lower tetramer populations (e.g. ΔN6, L65C-βME) showed differences across four regions of primary sequence (labelled 1-4 in Figure 5F and Figure S21). Regions 1-3 contain residues that either make up the tetramer interaction interfaces and/or have shifted significantly (≥ 4 Å root-mean-squared deviation; RMSD) in the crystal structure relative to monomeric ΔN6 (Figure 5D). While region 4 does not undergo any structural changes itself in the crystal structure, it is adjacent in three-dimensional space to a region which does (the BC loop), and so will experience a change in chemical environment upon tetramerization (Figure 5D).

In addition to the NMR data supporting the relevance of the S52C-S**54** crystal structure to oligomerization in solution, these data also indicate that the tetramers formed by the S52C- and L65C-fragment adducts are structurally similar. The ability of S52C- and L65C-fragment adducts to adopt highly similar tetrameric species can be rationalized in the context of the crystal structure. D strand straightening results in residues 52 and 65 now lying adjacent to one another, and so we anticipate that fragments tethered to the L65C variant of ΔN6 could access the same binding pockets which -S**54** is observed to occupy in the S52C-S**54** tetramer structure (Figure S17A).

Structural similarities of off-pathway ΔN6 tetramers to full-length β_2m oligomers. While similar regions of ΔN6 are involved in the formation of the tetramer and the previously identified on-pathway dimers and hexamers (which were characterized under similar conditions to those employed here)[37], the PPIs themselves are significantly different and mutually exclusive (Figure S22A). This observation rationalizes the off-pathway behavior of the tetramer, as it would need to completely dissociate in order to form the on-pathway hexamer. However, although the tetramer is different to previously identified ΔN6 oligomers[37,41,52], these interfaces bear resemblance to those associated with several full-length β_2m oligomers[53–56]. The most striking similarities are those to a crystallographic tetramer formed by the P32A variant (PDB 2F8O[53]; Figure S22B and S22C) – P32A β_2m is largely monomeric in solution[53] (in the absence of divalent copper[57]), but at the high concentrations within the crystal lattice then protein molecules can interact via the same D strand and ABED interfaces shown in Figure 5 (Figure S22B and S22C). Although the solution-relevance of the crystallographic P32A tetramer was never shown, the NMR data obtained for S52C-S**54** confirms that this arrangement of protomers is possible in solution, and stable in the presence of suitable ligands.

Whereas the crystallographic P32A β_2m tetramer possesses the same straight β strand as the S52C-S**54** ΔN6 tetramer, other β_2m oligomers for which high-resolution structural information is available lack straight D strands and instead involve DE and BC loop-mediated interactions[54–56]. As these oligomers have been shown or proposed to be on-pathway species, and as formation of a D sheet interface is incompatible with such loop-loop interactions (Figure S22A), we hypothesize that formation of an eight-stranded ABED-DEBA β-sheet, as observed for the S52C-S**54** ΔN6 tetramer and the β_2m P32A crystallographic tetramer, is an off-pathway interaction which can be driven by ligand binding across the ABED sheet (as for ΔN6 S52C-S54) or modulation of the BC loop (as for β_2m P32A).

CONCLUSIONS

Covalent small molecules are becoming increasingly attractive tools to modulate specific protein-protein interactions[43,44,58–60], to interrogate the role of different proteins in biological processes[44,58,61–63], and to facilitate structural studies of challenging targets[42,64]. The results presented here expand this covalent chemical tool approach, highlighting its power to facilitate analysis of the structure and role of specific oligomers in self-assembly pathways. We have demonstrated that covalently reinforced protein-ligand interactions[65–67] can be used to manipulate heterogeneous and dynamic PPIs, exemplified by those formed in the initial stages of amyloid formation, which are notoriously difficult to target specifically when using purely non-covalent approaches[68]. By assessing both the affinity of non-covalent interactions between a protein and covalent fragment, and the effect of these fragments on protein oligomerization, insights into the molecular basis of PPI modulation (i.e. whether it is due to non-covalent binding or surface functionalization) have been gained. Specifically, the use of disulfide tethering to identify covalent fragments uniquely allowed a transient off-pathway tetramer (as shown by kinetic data and models) of the amyloidogenic protein ΔN6 to be trapped and characterized in atomic detail for the first time. These results highlight the power of the chemical modification of proteins as a general strategy to manipulate complex self-assembling systems and drive the formation of defined oligomers for detailed study.

EXPERIMENTAL SECTION

Safety. No unexpected, new, and/or significant hazards or risks were associated with this research.

Disulfide tethering screening. Screening cocktails were prepared by combining five disulfide-linked fragments (1.25 mM each; all present as symmetrical disulfides) in the presence of βME (25 mM) in DMSO. These initial cocktail mixtures were incubated at ambient temperature (~18 °C) for 12 h to allow the formation of mixed disulfides with βME (which generally had improved aqueous solubility over the symmetrical disulfides).

Screening cocktails were diluted further into each ΔN6 cysteine variant (5 μM protein, with 25 μM each disulfide, 500 μM βME, 2% v/v DMSO) in 25 mM sodium phosphate at either pH 6.2 (main text data) or pH 8.0 (Supplementary Information data), and the resulting screening mixtures were incubated at ambient temperature. The distribution of covalent protein-fragment adducts over time was analyzed by a Bruker maXis Impact QTOF mass spectrometer, with an electrospray ionization source. Samples (1 μL injections) were desalted prior to mass spectrometry by an in-line Dionex UltiMate 3000 liquid chromatography system (Thermo Scientific), equipped with an Aeris Widepore C4 column (Phenomenex), running a gradient between water and acetonitrile, both supplemented with 0.1% formic acid.

MCL-1 (residues 172-327; purified as described previously[69]) was screened using the same procedure, but in 25 mM sodium phosphate pH 7.4.

Mass spectra were deconvoluted using a maximum entropy algorithm (DataAnalysis, Bruker). For each protein-fragment adduct in each cocktail, the intensity of the deconvoluted peak at 24 h was measured relative to the protein-βME adduct peak. These relative intensities were then converted to RZ scores[48]. The RZ score for the i-th fragment can be described by Equation 1:

$$\mathrm{RZ} = \frac{x_i - \mathrm{median}(x_{all})}{\mathrm{MAD}(x_{all})} \quad (1)$$

where x_i is the relative intensity of the protein-fragment adduct peak for fragment i, and x_{all} is a list of relative peak intensities for all protein-fragment adducts in that data set (i.e. for a given cysteine variant at a given pH). In all cases, peak intensities were measured relative to the βME adduct. The medium absolute deviation (MAD)[70] is defined as:

$$\mathrm{MAD}(x_{all}) = 1.4826 \times \mathrm{median}(|x_i\text{-}\mathrm{median}(x_{all})|) \quad (2)$$

RZ scores for the disulfide analogue of βME could not be determined by this method, due to the presence of βME as a reducing agent in all screening mixtures. Instead, its RZ score was estimated through competition experiments, as shown in Figure S7.

Sedimentation velocity analytical ultracentrifugation. Experiments were carried out at 48,000 rpm, 25 °C with at An50-Ti rotor in a Beckman Coulter Optima XL-I ultracentrifuge. Samples and reference buffer (400 µL) were loaded into 12 mm aluminium centerpieces, with sapphire windows. Samples were thermally equilibrated for 2-3 hours at 0 rpm and were subsequently analyzed using the interference detection system at a protein concentration of 150 µM in 25 mM sodium phosphate pH 6.2. All samples had been exhaustively dialyzed in this buffer prior to loading, and the dialysate was used as the reference buffer.

Data were analyzed in SEDFIT (version 12.44)[71] with a continuous *c*(*s*) distribution model and with a maximum entropy regularization confidence interval of 0.95. Values for the partial specific volume ($\bar{v}$) of ΔN6, buffer viscosity (η), and buffer density (ρ) were all calculated using SEDNTERP[72] ($\bar{v}$ = 0.72832 mL/g; η = 0.00898 P and ρ = 0.99954 g/mL for 25 mM sodium phosphate pH 6.2). Final fitting was performed with the Levenberg-Marquardt algorithm, although initial fitting was performed with both Simplex and Levenberg-Marquardt algorithms. For *c*(*s*) distributions with significant peak broadening or overlap, further processing was subsequently performed to permit baseline resolution of these peaks: multiple Gaussian functions were fit to the initial *c*(*s*) distribution (using the curve_fit function from SciPy.optimize), then the positions of these best fit Gaussians were used in SEDFIT as Bayesian prior expectations[73] (modelled again as Gaussians, located at the best-fit positions identified by curve_fit, with widths set to 0.2 and amplitudes set to 0.1). Refitting the data with the Levenberg-Marquardt algorithm led to improved or equally good root-mean-square deviations (compared to the original *c*(*s*) distribution) for all datasets to which this processing method had been applied, confirming the validity of this approach.

Peaks in the *c*(*s*) distributions were assigned to specific oligomers based on comparison to published ΔN6 SV-AUC data[37] and predicted sedimentation coefficients for these oligomers. Predicted sedimentation coefficients were calculated using the Svedberg equation[49] at a range of possible frictional ratios, so as to estimate the range of possible sedimentation coefficients which could describe a particle of a given molecular weight.

Thioflavin T aggregation assays. Protein-fragment adducts (150 µM) were incubated in 25 mM sodium phosphate pH 6.2 with 10 µM ThT, in the presence or absence of 15 µM (monomer equivalent) fibril seeds prepared from ΔN6, in 96-well untreated half-area plates (Corning; 100 µL sample per well). In the same plate, 15 µM (monomer equivalent) fibril seeds were incubated alone in 25 mM sodium phosphate pH 6.2. Details concerning the preparation of fibril seeds can be found in the Supporting Information.

Fibril elongation was allowed to occur quiescently, with brief agitation (10 sec at 600 rpm) only occurring prior to each reading (every 12 min). Experiments were performed for 24 h at 25 °C in a FLUOstar OPTIMA plate reader (BMG Labtech), exciting ThT at 444 nm and measuring its fluorescence emission intensity at 480 nm.

Data were processed by subtracting two data sets from each seeded data set to remove changes in ThT fluorescence which had occurred independently of fibril elongation: (a) data obtained from the same protein-fragment adduct in the absence of fibril seeds; and (b) data

obtained for fibril seeds alone in buffer. The absence of fibrillar aggregates in the unseeded samples after 24 h was confirmed by negative stain electron microscopy (see Supporting Information). Initial elongation rates from the processed seeded data sets were measured by fitting a straight line to the first 3 h of data and determining the slope of this line.

Protein crystallography and data processing. A stock solution of S52C-S**54** was prepared by incubation of S52C (1.5 mM) and Di-S**54** (1.5 mM) in 25 mM sodium phosphate pH 8.0, 725 μM βME, 20% v/v DMSO for 40 h at room temperature, before exhaustive dialysis against 25 mM sodium phosphate pH 6.2 at 4 °C, using dialysis tubes with a 3.5 kDa molecular weight cut-off (Generon). The concentration of the dialyzed sample was determined through a bicinchoninic acid (BCA) assay[74]. Crystals were grown by mixing 0.2 μL of the protein-fragment complex (1.1 mM) and 0.1 μL of the crystallization solution in hanging drop plates at 293 K. The crystallization solution was prepared using 0.1 M Morpheus Buffer System 3 at pH 8.5, 31% w/v Morpheus Precipitant Mix 4, and 0.04 M Morpheus Alcohols Mix (all from Molecular Dimensions) – this is equivalent to 53.4 mM bicine, 46.6 mM Tris, pH 8.5, 11% w/v PEG 3350, 11% w/v PEG 1000, 11% v/v 2-methyl-2,4-pentanediol, and 6.7 mM each of 1,6-hexanediol, 1-butanol, 1,2-propanediol, 2-propanol, 1,4-butanediol, and 1,3-propanediol). After 2 weeks, crystals were fished and flash-frozen in liquid nitrogen. The diffraction data was collected at 0.9795 Å, with 0.025 second exposition and 0.15° oscillation, for a total of 2400 images on beamline I24 at Diamond Light Source (UK). The data were processed using the xia2[75] bundle, with DIALS[76] for integration and using Pointless[77]/Aimless[78] for scaling and merging. The data were processed using CC1/2 and completeness as cutoff criteria[79]. The structure of S52C-**S54** was solved by molecular replacement, using full-length β_2m (PDB 5CS7[80]) with the first six amino acids removed as search model in PHASER[81]. COOT[82] and REFMAC5[83] were used for refinement. The quality of the final structure was assessed with MolProbity[84]. Data collection and refinement statistics are shown in Table S1. Figures were prepared using PyMOL (version 2.4, Schrödinger).

Protein NMR. All spectra were acquired using a 750 MHz Bruker Avance III HD spectrometer equipped with a TCI cryoprobe, at a protein concentration of 150 μM in 25 mM sodium phosphate pH 6.2, at 25 °C. ^{1}H-^{15}N-SOFAST-HMQC spectra were processed using NMRPipe[85], and calculation of peak intensities was performed in CcpNmr Analysis (version 2.4)[86]. ^{1}H-^{15}N peaks were assigned to specific backbone resonances for each protein-fragment adduct (L65C-βME, L65C-S**54**, S52C-βME, and S52C-S**54**) by comparison to existing ΔN6 assignments[36], only considering peaks with intensities at least three-fold greater than the spectral noise. Backbone chemical shift perturbations (CSPs) between samples were calculated using Equation 3:

$$\mathrm{CSP} = \sqrt{25\Delta\delta_{HN}{}^2 + \Delta\delta_N{}^2} \tag{3}$$

where $\Delta\delta_{HN}$ and $\Delta\delta_N$ represent the difference in peak position in the direct and indirect dimensions, respectively.

L65C-βME and L65C-S**54** T_2 experiments were performed by acquiring a series of sensitivity-enhanced ^{1}H-^{15}N-HSQC spectra in an interleaved fashion at a range of delay times (0.017-0.136 ms for L65C-βME, 0.017-0.119 ms for L65C-S**54**). Peak intensities (I) were extracted from each spectrum using the series.tab NMRPipe module, and per-residue ^{15}N relaxation rates (R_2) were calculated by fitting the peak intensity at different delay times (t) to a two-parameter exponential function (Equation 4).

$$I = -\mathrm{a}e^{-R_2 t} \tag{4}$$

For S52C-βME and S52C-S**54**, sensitivity limitations did not permit the determination of ^{15}N R_2 rates on a per-residue basis. Instead, the first increment of the standard T_2 experiment at each delay time (0.017-0.102 ms for S52C-βME, 0.017-0.085 ms S52C-S**54**) was used to determine the R_2 rate of the whole amide region (7.6-9.2 ppm). Mean ^{15}N R_2 rates for the whole amide region were calculated in the same way for ΔN6 (0.017-0.085 ms) and the two L65C adducts (L65C-βME and L65C-S**54**; using the same data sets acquired for determining per-residue ^{15}N R_2 rates).

ASSOCIATED CONTENT

- Supporting Information (PDF): Supplementary figures and tables, supplementary materials and methods (including protein expression and purification, computational solvent mapping, design and synthesis of the disulfide fragment library, preparation of individual protein-fragment adducts, preparation of ΔN6 fibril seeds for thioflavin T aggregation assays, and negative-stain transmission electron microscopy), and characterization of synthesized compounds
- The ΔN6 S52C-S**54** tetramer crystal structure has been deposited in the Protein Data Bank with the PDB code 7AFV

AUTHOR INFORMATION

Corresponding Author

*E-mail: S.E.Radford@leeds.ac.uk

*E-mail: A.J.Wilson@leeds.ac.uk

Author Contributions

E.E.C., S.E.R, and A.J.W. conceived and designed the research program, E.E.C. designed studies and performed the research with support from N. G. (crystallography), J.S.E. (AUC) and T.K.K. (NMR). The manuscript was written by E.E.C., S.E.R., and A.J.W. with contributions from all authors. E.E.C. prepared all figures.

Funding Sources

This work was supported by The Wellcome Trust (109154/Z/15/A, 204963, 109984, 097827/Z/11/A, WT094232MA, 094232/Z/10/Z, 108466/Z/15/Z and 094232/Z/10/Z), EPSRC (EP/N035267/1, EP/KO39292/1, EP/N013573/1), BBSRC (BB/M011151/1) and ERC (322408). A.J.W. holds a Royal Society Leverhulme Trust Senior Fellowship (SRF/R1/191087).

ACKNOWLEDGMENTS

The authors wish to thank Rodolfo Ghirlando for advice on SV-AUC procedures, data analysis, and interpretation, Pallavi Ramsahye for purification of the MCL-1 protein, Honghao Zhang and Zsófia Hegedüs for their work performing the MCL-1 tethering experiments, Arnout Kalvedra for assistance with NMR experiments, and Rodrigo Gallardo and Sabine Ulamec for their help obtaining EM micrographs. We thank all our group members especially those in the 'amyloid team' for many helpful discussions.

REFERENCES

(1) Pieters, B. J. G. E.; van Eldijk, M. B.; Nolte, R. J. M.; Mecinović, J. Natural supramolecular protein assemblies. *Chem. Soc. Rev.* **2016**, *45*, 24–39.

(2) Garcia-Seisdedos, H.; Villegas, J. A.; Levy, E. D. Infinite assembly of folded proteins in evolution, disease, and engineering. *Angew. Chemie Int. Ed.* **2019**, *58*, 5514–5531.

(3) Novo, M.; Freire, S.; Al-Soufi, W. Critical aggregation concentration for the formation of early amyloid-β (1-42) oligomers. *Sci. Rep.* **2018**, *8*, 1783.

(4) Owen, M. C.; Gnutt, D.; Gao, M.; Wärmländer, S. K. T. S.; Jarvet, J.; Gräslund, A.; Winter, R.; Ebbinghaus, S.; Strodel, B. Effects of in vivo conditions on amyloid aggregation. *Chem. Soc. Rev.* **2019**, *48*, 3946–3996.

(5) Stephens, A. D.; Zacharopoulou, M.; Kaminski Schierle, G. S. The cellular environment affects monomeric α-synuclein structure. *Trends Biochem. Sci.* **2019**, *44*, 453–466.

(6) Rodriguez Camargo, D. C.; Tripsianes, K.; Buday, K.; Franko, A.; Göbl, C.; Hartlmüller, C.; Sarkar, R.; Aichler, M.; Mettenleiter, G.; Schulz, M.; Böddrich, A.; Erck, C.; Martens, H.; Walch, A. K.; Madl, T.; Wanker, E. E.; Conrad, M.; Hrabě de Angelis, M.; Reif, B. The redox environment triggers conformational changes and aggregation of hIAPP in type II diabetes. *Sci. Rep.* **2017**, *7*, 44041.

(7) Garcia-Seisdedos, H.; Empereur-Mot, C.; Elad, N.; Levy, E. D. Proteins evolve on the edge of supramolecular self-assembly. *Nature*

2017, *548*, 244–247.

(8) De Baets, G.; Van Doorn, L.; Rousseau, F.; Schymkowitz, J. Increased aggregation is more frequently associated to human disease-associated mutations than to neutral polymorphisms. *PLoS Comput. Biol.* **2015**, *11*, e1004374.

(9) Park, S.; Lee, J. H.; Jeon, J. H.; Lee, M. J. Degradation or aggregation: the ramifications of post-translational modifications on tau. *BMB Rep.* **2018**, *51*, 265–273.

(10) Barykin, E. P.; Mitkevich, V. A.; Kozin, S. A.; Makarov, A. A. Amyloid β modification: a key to the sporadic Alzheimer's disease? *Front. Genet.* **2017**, *8*, 58.

(11) Sambataro, F.; Pennuto, M. Post-translational modifications and protein quality control in motor neuron and polyglutamine diseases. *Front. Mol. Neurosci.* **2017**, *10*, 82.

(12) Eaton, W. A.; Hofrichter, J. Sickle cell hemoglobin polymerization. *Adv. Protein Chem.* **1990**, *40*, 63–279.

(13) Chiti, F.; Dobson, C. M. Protein misfolding, amyloid formation, and human disease: a summary of progress over the last decade. *Annu. Rev. Biochem.* **2017**, *86*, 27–68.

(14) Iadanza, M. G.; Jackson, M. P.; Hewitt, E. W.; Ranson, N. A.; Radford, S. E. A new era for understanding amyloid structures and disease. *Nat. Rev. Mol. Cell Biol.* **2018**, *19*, 755–773.

(15) Kumar, S.; Henning-Knechtel, A.; Magzoub, M.; Hamilton, A. D. Peptidomimetic-based multidomain targeting offers critical evaluation of Aβ structure and toxic function. *J. Am. Chem. Soc.* **2018**, *140*, 6562–6574.

(16) Hoffmann, W.; Folmert, K.; Moschner, J.; Huang, X.; von Berlepsch, H.; Koksch, B.; Bowers, M. T.; von Helden, G.; Pagel, K. NFGAIL amyloid oligomers: the onset of beta-sheet formation and the mechanism for fibril formation. *J. Am. Chem. Soc.* **2018**, *140*, 244–249.

(17) Economou, N. J.; Giammona, M. J.; Do, T. D.; Zheng, X.; Teplow, D. B.; Buratto, S. K.; Bowers, M. T. Amyloid β-protein assembly and Alzheimer's disease: dodecamers of Aβ42, but not of Aβ40, seed fibril formation. *J. Am. Chem. Soc.* **2016**, *138*, 1772–1775.

(18) Hsieh, M.-C.; Liang, C.; Mehta, A. K.; Lynn, D. G.; Grover, M. A. Multistep conformation selection in amyloid assembly. *J. Am. Chem. Soc.* **2017**, *139*, 17007–17010.

(19) Salveson, P. J.; Haerianardakani, S.; Thuy-Boun, A.; Kreutzer, A. G.; Nowick, J. S. Controlling the oligomerization state of Aβ-derived peptides with light. *J. Am. Chem. Soc.* **2018**, *140*, 5842–5852.

(20) Mondal, S.; Jacoby, G.; Sawaya, M. R.; Arnon, Z. A.; Adler-Abramovich, L.; Rehak, P.; Vuković, L.; Shimon, L. J. W.; Král, P.; Beck, R.; Gazit, E. Transition of metastable cross-α crystals into cross-β fibrils by β-turn flipping. *J. Am. Chem. Soc.* **2019**, *141*, 363–369.

(21) Eisele, Y. S.; Monteiro, C.; Fearns, C.; Encalada, S. E.; Wiseman, R. L.; Powers, E. T.; Kelly, J. W. Targeting protein aggregation for the treatment of degenerative diseases. *Nat. Rev. Drug Discov.* **2015**, *14*, 759–780.

(22) Seroski, D. T.; Hudalla, G. A. Self-assembled peptide and protein nanofibers for biomedical applications. In *Biomedical Applications of Functionalized Nanomaterials: Concepts, Development and Clinical Translation*; Elsevier Inc.: Amsterdam, 2018; pp 569–598.

(23) Adler-Abramovich, L.; Gazit, E. The physical properties of supramolecular peptide assemblies: from building block association to technological applications. *Chem. Soc. Rev.* **2014**, *43*, 6881–6893.

(24) Breydo, L.; Uversky, V. N. Structural, morphological, and functional diversity of amyloid oligomers. *FEBS Lett.* **2015**, *589*, 2640–2648.

(25) Kjaergaard, M.; Dear, A. J.; Kundel, F.; Qamar, S.; Meisl, G.; Knowles, T. P. J.; Klenerman, D. Oligomer diversity during the aggregation of the repeat region of tau. *ACS Chem. Neurosci.* **2018**, *9*, 3060–3071.

(26) Wilson, C. G.; Arkin, M. R. Probing structural adaptivity at PPI interfaces with small molecules. *Drug Discov. Today Technol.* **2013**, *10*, e501–e508.

(27) Krall, N.; da Cruz, F. P.; Boutureira, O.; Bernardes, G. J. L. Site-selective protein-modification chemistry for basic biology and drug development. *Nat. Chem.* **2016**, *8*, 103–113.

(28) Wright, T. H.; Bower, B. J.; Chalker, J. M.; Bernardes, G. J. L.; Wiewiora, R.; Ng, W. L.; Raj, R.; Faulkner, S.; Vallée, M. R. J.; Phanumartwiwath, A.; Coleman, O. D.; Thézénas, M.-L.; Khan, M.; Galan, S. R. G.; Lercher, L.; Schombs, M. W.; Gerstberger, S.; Palm-Espling, M. E.; Baldwin, A. J.; Kessler, B. M.; Claridge, T. D. W.; Mohammed, S.; Davis, B. G. Posttranslational mutagenesis: a chemical strategy for exploring protein side-chain diversity. *Science* **2016**, *354*, aag1465.

(29) van Hateren, A.; Bailey, A.; Elliott, T. Recent advances in Major Histocompatibility Complex (MHC) class I antigen presentation: plastic MHC molecules and TAPBPR-mediated quality control. *F1000Research* **2017**, *6*, 158.

(30) Iadanza, M. G.; Silvers, R.; Boardman, J.; Smith, H. I.; Karamanos, T. K.; Debelouchina, G. T.; Su, Y.; Griffin, R. G.; Ranson, N. A.; Radford, S. E. The structure of a β2-microglobulin fibril suggests a molecular basis for its amyloid polymorphism. *Nat. Commun.* **2018**, *9*, 4517.

(31) Eichner, T.; Radford, S. E. Understanding the complex mechanisms of β2-microglobulin amyloid assembly. *FEBS J.* **2011**, *278*, 3868–3883.

(32) Scarpioni, R.; Ricardi, M.; Albertazzi, V.; De Amicis, S.; Rastelli, F.; Zerbini, L. Dialysis-related amyloidosis: challenges and solutions. *Int. J. Nephrol. Renovasc. Dis.* **2016**, *9*, 319–328.

(33) Gejyo, F.; Yamada, T.; Odani, S.; Nakagawa, Y.; Arakawa, M.; Kunitomo, T.; Kataoka, H.; Suzuki, M.; Hirasawa, Y.; Shirahama, T.; Cohen, A. S.; Schmid, K. A new form of amyloid protein associated with chronic hemodialysis was identified as β2-microglobulin. *Biochem. Biophys. Res. Commun.* **1985**, *129*, 701–706.

(34) Bellotti, V.; Stoppini, M.; Mangione, P.; Sunde, M.; Robinson, C.; Asti, L.; Brancaccio, D.; Ferri, G. B2-microglobulin can be

refolded into a native state from ex vivo amyloid fibrils. *Eur. J. Biochem.* **1998**, *258*, 61–67.

(35) Stoppini, M.; Arcidiaco, P.; Mangione, P.; Giorgetti, S.; Brancaccio, D.; Bellotti, V. Detection of fragments of β2-microglobulin in amyloid fibrils. *Kidney Int.* **2000**, *57*, 349–350.

(36) Eichner, T.; Kalverda, A. P.; Thompson, G. S.; Homans, S. W.; Radford, S. E. Conformational conversion during amyloid formation at atomic resolution. *Mol. Cell* **2011**, *41*, 161–172.

(37) Karamanos, T. K.; Jackson, M. P.; Calabrese, A. N.; Goodchild, S. C.; Cawood, E. E.; Thompson, G. S.; Kalverda, A. P.; Hewitt, E. W.; Radford, S. E. Structural mapping of oligomeric intermediates in an amyloid assembly pathway. *Elife* **2019**, *8*, e46574.

(38) Su, Y.; Sarell, C. J.; Eddy, M. T.; Debelouchina, G. T.; Andreas, L. B.; Pashley, C. L.; Radford, S. E.; Griffin, R. G. Secondary structure in the core of amyloid fibrils formed from human β2m and its truncated variant ΔN6. *J. Am. Chem. Soc.* **2014**, *136*, 6313–6325.

(39) Karamanos, T. K.; Kalverda, A. P.; Thompson, G. S.; Radford, S. E. Visualization of transient protein-protein interactions that promote or inhibit amyloid assembly. *Mol. Cell* **2014**, *55*, 214–226.

(40) Rennella, E.; Cutuil, T.; Schanda, P.; Ayala, I.; Gabel, F.; Forge, V.; Corazza, A.; Esposito, G.; Brutscher, B. Oligomeric states along the folding pathways of β2-microglobulin: kinetics, thermodynamics, and structure. *J. Mol. Biol.* **2013**, *425*, 2722–2736.

(41) Domanska, K.; Vanderhaegen, S.; Srinivasan, V.; Pardon, E.; Dupeux, F.; Marquez, J. A.; Giorgetti, S.; Stoppini, M.; Wyns, L.; Bellotti, V.; Steyaert, J. Atomic structure of a nanobody-trapped domain-swapped dimer of an amyloidogenic β2-microglobulin variant. *Proc. Natl. Acad. Sci. U. S. A.* **2011**, *108*, 1314–1319.

(42) Wang, N.; Majmudar, C. Y.; Pomerantz, W. C.; Gagnon, J. K.; Sadowsky, J. D.; Meagher, J. L.; Johnson, T. K.; Stuckey, J. A.; Brooks III, C. L.; Wells, J. A.; Mapp, A. K. Ordering a dynamic protein via a small molecule stabilizer. *J. Am. Chem. Soc.* **2013**, *135*, 3363–3366.

(43) Sijbesma, E.; Hallenbeck, K. K.; Leysen, S.; de Vink, P. J.; Skóra, L.; Jahnke, W.; Brunsveld, L.; Arkin, M. R.; Ottmann, C. Site-directed fragment-based screening for the discovery of protein-protein interaction stabilizers. *J. Am. Chem. Soc.* **2019**, *141*, 3524–3531.

(44) Lee, S.; Wales, T. E.; Escudero, S.; Cohen, D. T.; Luccarelli, J.; Gallagher, C. G.; Cohen, N. A.; Huhn, A. J.; Bird, G. H.; Engen, J. R.; Walensky, L. D. Allosteric inhibition of antiapoptotic MCL-1. *Nat. Struct. Mol. Biol.* **2016**, *23*, 600–607.

(45) Hall, Z.; Schmidt, C.; Politis, A. Uncovering the early assembly mechanism for amyloidogenic β2-microglobulin using cross-linking and native mass spectrometry. *J. Biol. Chem.* **2016**, *291*, 4626–4637.

(46) Kozakov, D.; Grove, L. E.; Hall, D. R.; Bohnuud, T.; Mottarella, S. E.; Luo, L.; Xia, B.; Beglov, D.; Vajda, S. The FTMap family of web servers for determining and characterizing ligand-binding hot spots of proteins. *Nat. Protoc.* **2015**, *10*, 733–755.

(47) Erlanson, D. A.; Braisted, A. C.; Raphael, D. R.; Randal, M.; Stroud, R. M.; Gordon, E. M.; Wells, J. A. Site-directed ligand discovery. *Proc. Natl. Acad. Sci. U. S. A.* **2000**, *97*, 9367–9372.

(48) Goktug, A. N.; Chai, S. C.; Chen, T. Data analysis approaches in high throughput screening. In *Drug Discovery*; IntechOpen, 2013; pp 201–226.

(49) Svedberg, T.; Pedersen, K. O. *The Ultracentrifuge*; Oxford University Press: Oxford, 1940.

(50) Xue, C.; Lin, T. Y.; Chang, D.; Guo, Z. Thioflavin T as an amyloid dye: fibril quantification, optimal concentration and effect on aggregation. *R. Soc. Open Sci.* **2017**, *4*, 160696.

(51) Biancalana, M.; Koide, S. Molecular mechanism of Thioflavin-T binding to amyloid fibrils. *Biochim. Biophys. Acta* **2010**, *1804*, 1405–1412.

(52) Hall, D.; Zhao, R.; So, M.; Adachi, M.; Rivas, G.; Carver, J. A.; Goto, Y. Recognizing and analyzing variability in amyloid formation kinetics: Simulation and statistical methods. *Anal. Biochem.* **2016**, *510*, 56–71.

(53) Eakin, C. M.; Berman, A. J.; Miranker, A. D. A native to amyloidogenic transition regulated by a backbone trigger. *Nat. Struct. Mol. Biol.* **2006**, *13*, 202–208.

(54) Calabrese, M. F.; Eakin, C. M.; Wang, J. M.; Miranker, A. D. A regulatable switch mediates self-association in an immunoglobulin fold. *Nat. Struct. Mol. Biol.* **2008**, *15*, 965–971.

(55) Colombo, M.; De Rosa, M.; Bellotti, V.; Ricagno, S.; Bolognesi, M. A recurrent D-strand association interface is observed in β-2 microglobulin oligomers. *FEBS J.* **2012**, *279*, 1131–1143.

(56) Halabelian, L.; Relini, A.; Barbiroli, A.; Penco, A.; Bolognesi, M.; Ricagno, S. A covalent homodimer probing early oligomers along amyloid aggregation. *Sci. Rep.* **2015**, *5*, 14651.

(57) Blaho, D. V.; Miranker, A. D. Delineating the conformational elements responsible for Cu 2+-induced oligomerization of β-2 microglobulin. *Biochemistry* **2009**, *48*, 6610–6617.

(58) Wang, N.; Lodge, J. M.; Fierke, C. A.; Mapp, A. K. Dissecting allosteric effects of activator-coactivator complexes using a covalent small molecule ligand. *Proc. Natl. Acad. Sci. U. S. A.* **2014**, *111*, 12061–12066.

(59) Ruiz, J.; Boehringer, R.; Grogg, M.; Raya, J.; Schirer, A.; Crucifix, C.; Hellwig, P.; Schultz, P.; Torbeev, V. Covalent tethering and residues with bulky hydrophobic side chains enable self-assembly of distinct amyloid structures. *ChemBioChem* **2016**, *17*, 2274–2285.

(60) Cardoso, R.; Love, R.; Nilsson, C. L.; Bergqvist, S.; Nowlin, D.; Yan, J.; Liu, K. K.-C.; Zhu, J.; Chen, P.; Deng, Y.-L.; Dyson, H. J.; Greig, M. J.; Brooun, A. Identification of Cys255 in HIF-1α as a novel site for development of covalent inhibitors of HIF-1α/ARNT PasB domain protein-protein interaction. *Protein Sci.* **2012**, *21*, 1885–1896.

(61) Backus, K. M.; Correia, B. E.; Lum, K. M.; Forli, S.; Horning, B. D.; González-Páez, G. E.; Chatterjee, S.; Lanning, B. R.; Teijaro, J. R.; Olson, A. J.; Wolan, D. W.; Cravatt, B. F. Proteome-wide covalent ligand discovery in native biological systems. *Nature*

2016, *534*, 570–574.

(62) Sadowsky, J. D.; Burlingame, M. A.; Wolan, D. W.; McClendon, C. L.; Jacobson, M. P.; Wells, J. A. Turning a protein kinase on or off from a single allosteric site via disulfide trapping. *Proc. Natl. Acad. Sci. U. S. A.* **2011**, *108*, 6056–6061.

(63) Ostrem, J. M.; Peters, U.; Sos, M. L.; Wells, J. A.; Shokat, K. M. K-Ras(G12C) inhibitors allosterically control GTP affinity and effector interactions. *Nature* **2013**, *503*, 548–551.

(64) Weichert, D.; Kruse, A. C.; Manglik, A.; Hiller, C.; Zhang, C.; Hübner, H.; Kobilka, B. K.; Gmeiner, P. Covalent agonists for studying G protein-coupled receptor activation. *Proc. Natl. Acad. Sci. U. S. A.* **2014**, *111*, 10744–10748.

(65) Krishnamurthy, V. M.; Semetey, V.; Bracher, P. J.; Shen, N.; Whitesides, G. M. Dependence of effective molarity on linker length for an intramolecular protein-ligand system. *J. Am. Chem. Soc.* **2007**, *129*, 1312–1320.

(66) Zhou, H.-X. Quantitative relation beteen intermolecular and intramolecular binding of Pro-rich peptides to SH3 domains. *Biophys. J.* **2006**, *91*, 3170–3181.

(67) Dal Corso, A.; Catalano, M.; Schmid, A.; Scheuermann, J.; Neri, D. Affinity enhancement of protein ligands by reversible covalent modification of neighboring lysine residues. *Angew. Chemie Int. Ed.* **2018**, *57*, 17178–17182.

(68) Young, L. M.; Ashcroft, A. E.; Radford, S. E. Small molecule probes of protein aggregation. *Curr. Opin. Chem. Biol.* **2017**, *39*, 90–99.

(69) Miles, J. A.; Yeo, D. J.; Rowell, P.; Rodriguez-Marin, S.; Pask, C. M.; Warriner, S. L.; Edwards, T. A.; Wilson, A. J. Hydrocarbon constrained peptides – understanding preorganisation and binding affinity. *Chem. Sci.* **2016**, *7*, 3694–3702.

(70) Chung, N.; Zhang, X. D.; Kreamer, A.; Locco, L.; Kuan, P. F.; Bartz, S.; Linsley, P. S.; Ferrer, M.; Strulovici, B. Median absolute deviation to improve hit selection for genome-scale RNAi screens. *J. Biomol. Screen.* **2008**, *13*, 149–158.

(71) Schuck, P. Size-distribution analysis of macromolecules by sedimentation velocity ultracentrifugation and Lamm equation modeling. *Biophys. J.* **2000**, *78*, 1606–1619.

(72) Hurton, T.; Wright, A.; Deubler, G.; Bashir, B. SEDNTERP. Computer program, downloaded from http://bitc.unh.edu, 2012.

(73) Brown, P. H.; Balbo, A.; Schuck, P. Using prior knowledge in the determination of macromolecular size-distributions by analytical ultracentrifugation. *Biomacromolecules* **2007**, *8*, 2011–2024.

(74) Smith, P. K.; Krohn, R. I.; Hermanson, G. T.; Mallia, A. K.; Gartner, F. H.; Provenzano, M. D.; Fujimoto, E. K.; Goeke, N. M.; Olson, B. J.; Klenk, D. C. Measurement of protein using bicinchroninic acid. *Anal. Biochem.* **1985**, *150*, 76–85.

(75) Winter, G. Xia2: An expert system for macromolecular crystallography data reduction. *J. Appl. Crystallogr.* **2010**, *43*, 186–190.

(76) Winter, G.; Waterman, D. G.; Parkhurst, J. M.; Brewster, A. S.; Gildea, R. J.; Gerstel, M.; Fuentes-Montero, L.; Vollmar, M.; Michels-Clark, T.; Young, I. D.; Sauter, N. K.; Evans, G. DIALS: Implementation and evaluation of a new integration package. *Acta Crystallogr. Sect. D Struct. Biol.* **2018**, *74*, 85–97.

(77) Evans, P. Scaling and assessment of data quality. *Acta Crystallogr. Sect. D Biol. Crystallogr.* **2006**, *62*, 72–82.

(78) Evans, P. R.; Murshudov, G. N. How good are my data and what is the resolution? *Acta Crystallogr. Sect. D Biol. Crystallogr.* **2013**, *69*, 1204–1214.

(79) Karplus, P. A.; Diederichs, K. Linking Crystallographic Model and Data Quality. *Science* **2012**, *336*, 1030–1033.

(80) Le Marchand, T.; de Rosa, M.; Salvi, N.; Sala, B. M.; Andreas, L. B.; Barbet-Massin, E.; Sormanni, P.; Barbiroli, A.; Porcari, R.; Mota, C. S.; de Sanctis, D.; Bolognesi, M.; Emsley, L.; Bellotti, V.; Blackledge, M.; Camilloni, C.; Pintacuda, G.; Ricagno, S. Conformational dynamics in crystals reveal the molecular bases for D76N beta-2 microglobulin aggregation propensity. *Nat. Commun.* **2018**, *9*, 1658.

(81) McCoy, A. J.; Grosse-Kunstleve, R. W.; Adams, P. D.; Winn, M. D.; Storoni, L. C.; Read, R. J. Phaser crystallographic software. *J. Appl. Crystallogr.* **2007**, *40*, 658–674.

(82) Emsley, P.; Lohkamp, B.; Scott, W. G.; Cowtan, K. Features and development of Coot. *Acta Crystallogr. Sect. D Biol. Crystallogr.* **2010**, *66*, 486–501.

(83) Murshudov, G. N.; Skubák, P.; Lebedev, A. A.; Pannu, N. S.; Steiner, R. A.; Nicholls, R. A.; Winn, M. D.; Long, F.; Vagin, A. A. REFMAC5 for the refinement of macromolecular crystal structures. *Acta Crystallogr. Sect. D Biol. Crystallogr.* **2011**, *67*, 355–367.

(84) Chen, V. B.; Arendall, W. B.; Headd, J. J.; Keedy, D. A.; Immormino, R. M.; Kapral, G. J.; Murray, L. W.; Richardson, J. S.; Richardson, D. C. MolProbity: All-atom structure validation for macromolecular crystallography. *Acta Crystallogr. Sect. D Biol. Crystallogr.* **2010**, *66*, 12–21.

(85) Delaglio, F.; Grzesiek, S.; Vuister, G. W.; Zhu, G.; Pfeifer, J.; Bax, A. NMRPipe: a multidimensional spectral processing system based on UNIX pipes. *J. Biomol. NMR* **1995**, *6*, 277–293.

(86) Vranken, W. F.; Boucher, W.; Stevens, T. J.; Fogh, R. H.; Pajon, A.; Llinas, M.; Ulrich, E. L.; Markley, J. L.; Ionides, J.; Laue, E. D. The CCPN data model for NMR spectroscopy: development of a software pipeline. *Proteins Struct. Funct. Bioinforma.* **2005**, *59*, 687–696.